Geophysical Journal International

Geophys. J. Int. (2021) **227,** 1496–1511
Advance Access publication 2021 July 21
GJI Seismology

https://doi.org/10.1093/gji/ggab285

A systematic investigation of piercing-point-dependent seismic azimuthal anisotropy

Yan Jia,[1] Kelly H. Liu,[1] Fansheng Kong,[1,2] Lin Liu[1,3,4] and Stephen S. Gao [1]

[1] *Geology and Geophysics Program, Missouri University of Science and Technology, Rolla, MO* 65409, *USA. E-mail: sgao@mst.edu*
[2] *Key Laboratory of Submarine Geosciences, Second Institute of Oceanography, Ministry of Natural Resources, Hangzhou* 310012, *China*
[3] *Frontiers Science Center for Deep Ocean Multispheres and Earth System, Key Lab of Submarine Geosciences and Prospecting Techniques, MOE and College of Marine Geosciences, Ocean University of China, Qingdao* 266100, *China*
[4] *Department of Geophysics, Stanford University, Stanford, CA* 94305, *USA*

Accepted 2021 July 17. Received 2021 July 15; in original form 2021 January 28

SUMMARY

The vast majority of teleseismic XKS (including SKS, SKKS and PKS) shear wave splitting studies interpret the observed splitting parameters (fast orientation and splitting time) based on the assumption of a spatially invariant anisotropy structure in the vicinity of a recording station. For such anisotropy structures the observed splitting parameters are either independent of the arriving azimuth of the seismic ray paths if the medium traversed by the ray paths can be represented by a single layer of anisotropy with a horizontal axis of symmetry (i.e. simple anisotropy), or demonstrate a periodic variation with respect to the arriving azimuth for a more complicated structure of anisotropy (e.g. multiple layers with a horizontal axis of symmetry, or a single layer with a dipping axis). When a recording station is located near the boundary of two or more regions with different anisotropy characteristics, the observed splitting parameters are dependent on the location of the ray piercing points. Such a piercing-point dependence is clearly observed using a total of 360 pairs of XKS splitting parameters at three stations situated near the northeastern edge of the Sichuan Basin in central China. For a given station, the fast orientations differ as much as 90°, and the azimuthal variation of the fast orientations lacks a 90° or 180° periodicity which is expected for double-layered or dipping axis anisotropy. The observed splitting parameters from the three stations are spatially most consistent when they are projected at a depth of ∼250 km, and can be explained by shear strain associated with the absolute plate motion and mantle flow deflected by the cone-shaped lithospheric root of the Sichuan Basin.

Key words: Mantle processes; Asia; Body wave; Computational seismology; Seismic anisotropy.

1 INTRODUCTION

Numerous observational and laboratory studies over the past several decades have suggested that the azimuthal dependence of seismic wave-speed, that is azimuthal anisotropy, is a nearly ubiquitous property of the Earth's upper mantle (e.g. Hess 1964; Francis 1969; Leven *et al.* 1981; Mainprice & Nicolas 1989; Silver & Chan 1991; Gao *et al.* 1994; Savage 1999; Long & Silver 2008, 2009; Yang *et al.* 2017). One of the most commonly used techniques to investigate azimuthal anisotropy is shear wave splitting (SWS) analysis (Fuchs 1977; Ando *et al.* 1983; Silver & Chan 1991; Vinnik *et al.* 1992; Silver 1996; Savage 1999; Long & Silver 2009). Numerous theoretical and observational studies demonstrate that when a shear wave propagates through a transversely isotropic medium, it splits into two quasi-shear waves with orthogonal polarization orientations propagating at different wave-speeds (Silver 1996; Savage 1999; Long & Silver 2009). The orientation and the strength of the anisotropy for a transversely isotropic medium are quantified by two splitting parameters, the polarization orientation of the fast wave (ϕ or fast orientation) and the delay time between the fast and slow waves (δt or splitting time). The most frequently employed seismic phases for SWS analysis are SKS, SKKS and PKS (hereafter referred to as XKS collectively), which are *P*-to-*S* converted waves at the core–mantle boundary on the receiver side (Ando *et al.* 1980; Silver & Chan 1991). Due to the steep angle of incidence of the XKS phases, the resulting splitting parameters possess high lateral resolution but low vertical resolution.

While the splitting parameters measured at a given station can usually be determined reliably, the interpretation of the observed splitting parameters is less trivial and frequently debated (e.g. Gao *et al.* 2010). Laboratory and geodynamic modelling investigations suggest that

strain-induced lattice preferred orientation (LPO) of anisotropic minerals (principally olivine) is mostly responsible for mantle azimuthal anisotropy (Zhang & Karato 1995). Specifically, in the upper asthenosphere, simple shear strain induced by the relative movement between the lithosphere and asthenosphere tends to align the *a*-axis of olivine subparallel to the relative movement direction between the two rheologically contrasting layers (Ben Ismail & Mainprice 1998; Long & Silver 2009; Ohuchi & Irifune 2013), while anisotropy of the lithosphere is generally related to vertically coherent deformation caused by horizontal compression, with the fast orientation being perpendicular to the maximum horizontal shortening direction (Silver & Chan 1991; Silver 1996; Fouch & Rondenay 2006). As a result of the non-uniqueness of the LPO-forming processes, the geodynamic implication of SWS observations for a given area is usually ambiguous. Therefore, exploring effective approaches for elucidating anisotropy-forming mechanisms is essential, not only for understanding the origin of seismic anisotropy but also for characterizing past or current deformational processes in the mantle.

The vast majority of the previous SWS studies measure and interpret the splitting parameters based on the assumption of simple anisotropy, which is characterized by a single layer of azimuthal anisotropy with a horizontal axis of symmetry (Silver & Savage 1994). In this ideal and frequently observed scenario, the anisotropic properties can be objectively reflected by the station-averaged splitting parameters because the individual splitting parameters do not vary with the backazimuth (arriving azimuth or BAZ) of the events. Any significant departure from the simple anisotropy characteristics can result in complex anisotropy. For most complex anisotropy cases, the observed splitting parameters are systematic functions of the BAZ of the seismic events (Silver & Savage 1994; Rumpker & Silver 1998). The most common form of complex anisotropy adopted is the two-layer model, which is composed of two anisotropic layers with non-parallel and non-orthogonal horizontal axes of symmetry. The individual splitting parameters in a two-layer model vary systematically against the BAZ, with a period of 90° (Silver & Savage 1994).

Besides complex anisotropy, another anisotropic structure that can result in azimuthal variation of the splitting parameters is piercing-point-dependent anisotropy. This type of anisotropy can be found when a recording station is situated near the boundary between two or more regions of simple anisotropy with different anisotropic characteristics (Liu & Gao 2013). The observed fast orientations and/or splitting times at the station vary as functions of ray piercing locations. Similar to complex anisotropy, station-averaged splitting parameters obtained in areas with piercing-point-dependent simple anisotropy cannot objectively represent the actual anisotropic properties. One excellent example of this type of seismic anisotropy is found at Station ENH which is located in Enshi City, Hubei Province, China (Fig. 1). Among the 61 pairs of XKS splitting measurements obtained at this station (Liu & Gao 2013), the BAZ for 28 pairs is between 111° and 124°, and the fast orientations and splitting times of these measurements have a mean value of 61.0 ± 11.0° and 0.61 ± 0.17 s, respectively. In comparison, the 33 measurements from events from the west and northwest have mean splitting parameters of 136.6 ± 15.1° and 0.79 ± 0.20 s.

Some previous SWS studies have also measured SWS parameters at Station ENH and surrounding stations (Fig. 1). Almost all of them only used SKS events which were dominantly located in the subduction zone of the western Pacific Ocean with a narrow BAZ range of about 110°–130° (Iidaka & Niu 2001; Luo *et al.* 2004; Zhao *et al.* 2007, 2011, 2013; Wang *et al.* 2013; Li *et al.* 2018; Yang *et al.* 2019). Consequently, the fast orientations from these studies are dominantly NE–SW or ENE–WSW (Fig. 1b). The limited BAZ coverage and the assumption of simple anisotropy led to controversial conclusions about the geodynamic implications of the splitting measurements among the previous studies. In this study, we conduct a systematic analysis using an updated data set from ENH and data from two nearby stations to systematically investigate piercing-point-dependent anisotropy and to estimate the depth of the source of the observed anisotropy by utilizing the piercing-point dependence of the splitting parameters.

2 DATA AND METHOD

The teleseismic seismic data set used in this study was recorded by three permanent broad-band stations, locate between 108.0°E–110.5°E and 29.5°N–31.0°N (Fig. 1). Data from station ENH were obtained from the Incorporated Research Institutions for Seismology (IRIS) Data Management Center (DMC), recorded over a 27-yr period from 1992 to 2019, and those from stations HFE and LCH were obtained from the Data Management Centre of China National Seismic Network at the Institute of Geophysics, China Earthquake Administration, with a recording duration spanning from July 2007 to September 2019 (Zheng *et al.* 2010).

The splitting parameters are measured and ranked using the procedure detailed in Liu *et al.* (2008) and Liu & Gao (2013), which is based on the method of minimization of the transverse energy technique (Silver & Chan 1991). The epicentral distance ranges used for data requesting are 120°–180°, 95°–180° and 84°–180° for PKS, SKKS and SKS, respectively. The minimum cut-off magnitude of the seismograms is 5.6 for events shallower than 100 km, and 5.5 for deeper events (Liu & Gao 2013). All the seismograms are initially bandpass filtered with corner frequencies of 0.04 and 0.5 Hz to enhance the signal-to-noise ratio (S/R) in the XKS phases. The beginning and the ending times of the XKS window are initially set as $T_{XKS} - 5.0$ s and $T_{XKS} + 20$ s, where T_{XKS} is the theoretical arrival time of the XKS phase computed using the IASP91 Earth model (Kennett & Engdahl 1991).

Following an S/N based ranking algorithm (Liu *et al.* 2008), the processed measurements are classified into four ranks as A (outstanding), B (good), C (bad) and N (null, for which XKS energy is only observed on the radial component but not on the transverse component). The splitting parameters, including the fast orientation (ϕ) and splitting time (δt), are initially determined automatically. Subsequently, the quality ranking, the beginning and ending times of the XKS window, and the bandpass filtering frequencies are visually verified and manually adjusted when necessary. In total, 289 teleseismic events are found to have resulted in at least one well-defined (A or B ranking) SWS measurement after the manual checking (Fig. 2a). Fig. 3 shows examples of quality 'A' measurements, which demonstrate significant BAZ dependence

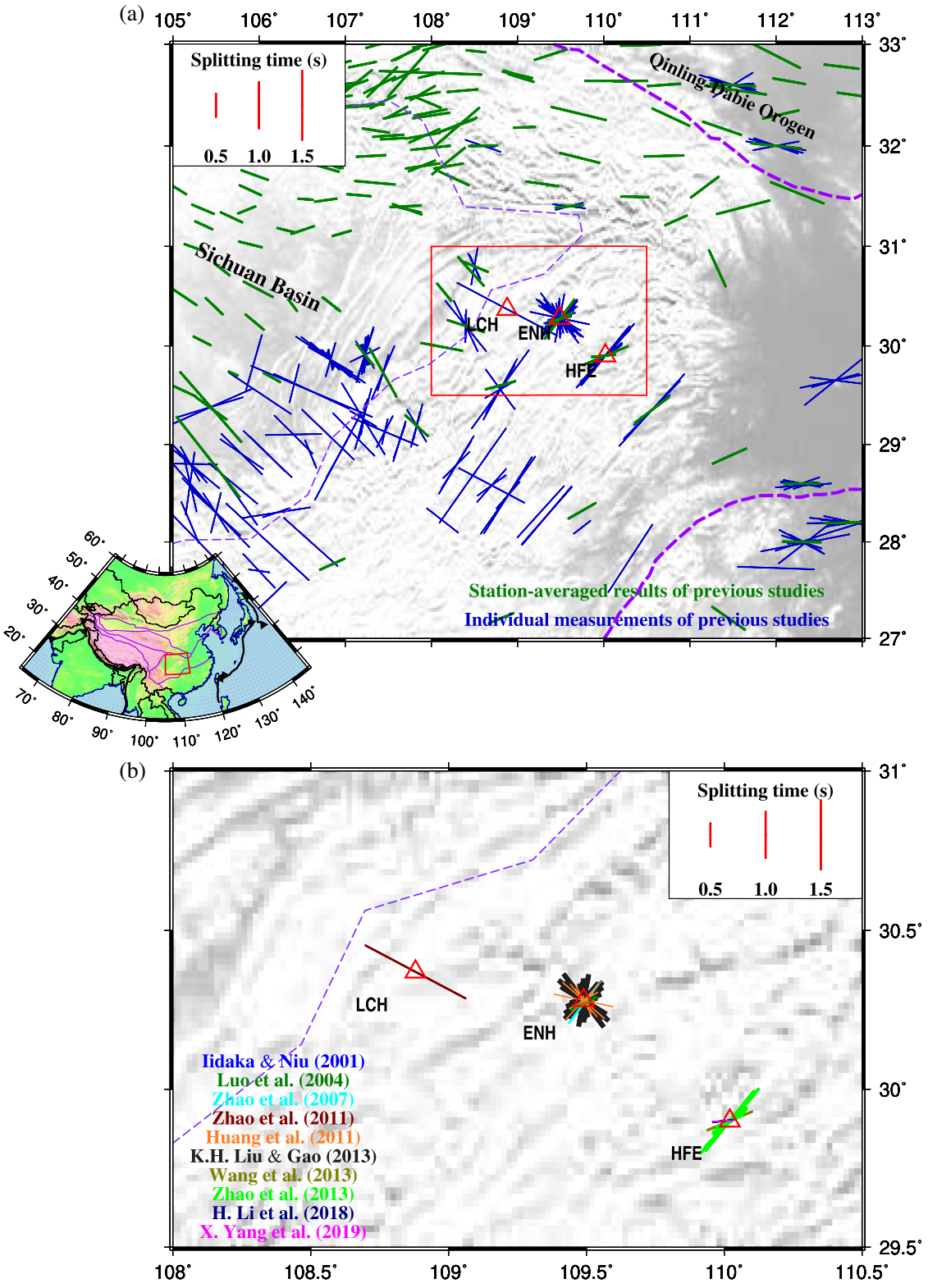

Figure 1. (a) Topographic map of the northeastern part of the Sichuan Basin showing major tectonic boundaries (thick purple dashed lines) and stations used in this study (red triangles with station name). The mapped area is marked by the red rectangle in the inset map of East Asia. The thin purple dashed line presents the boundary of the Sichuan Basin. The thick green and thin blue bars indicate the station-averaged and individual shear wave splitting (SWS) measurements from different previous studies obtained from http://www.gm.univ-montp2.fr/splitting/DB/. (b) Previous SWS measurements at stations used in this study. Different colours represent different studies.

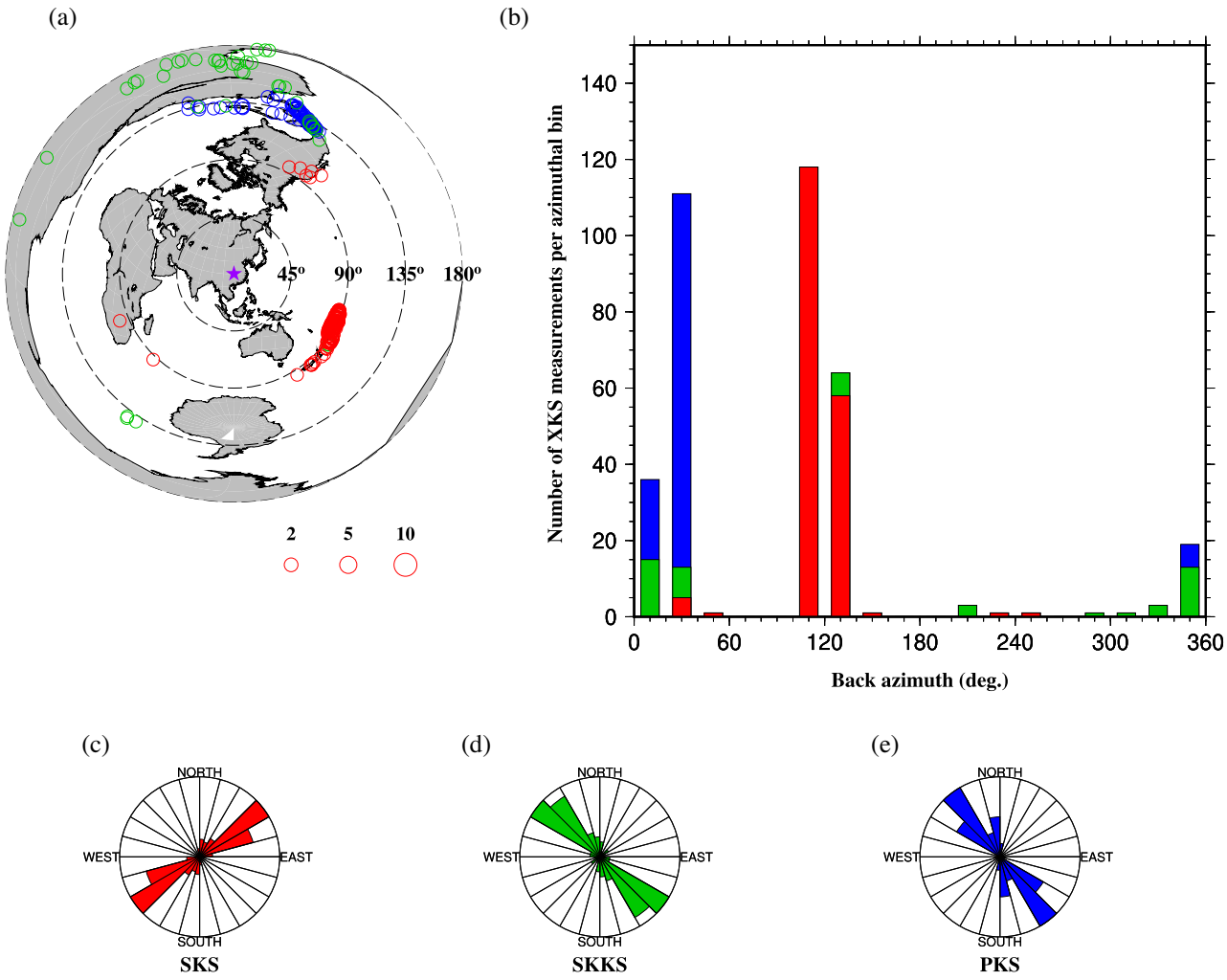

Figure 2. Events location. (a) An azimuthal equidistant projection map showing the spatial distribution of the earthquakes (circles) centred at the study area (purple star). The radius of the circles is proportional to the number of quality A or B SWS measurements from the events. (b) A histogram of the backazimuthal distribution measured by the SWS measurements. (c–e) Rose diagrams illustrating the fast orientations of the SKS, SKKS and PKS phases. For all the plots, red, green and blue colours represent the SKS, SKKS and PKS events or measurements.

of the splitting parameters obtained at the same stations. The uncertainties in the individual measurements are estimated using the *F*-test approach specified in Silver & Chan (1991) and represent one standard deviation. The mean splitting time and its uncertainty at a given station or a given area are estimated using the arithmetic average and its standard deviation over all the individual measurements, and the mean fast orientation and its uncertainty are computed using the circular mean and circular standard deviation (Mardia & Jupp 2000; Gao *et al.* 2008).

3 RESULTS AND COMPARISON WITH MEASUREMENTS FROM PREVIOUS STUDIES

A total of 360 pairs of well-defined splitting measurements were obtained, including 191 from Station ENH (Fig. 4), 78 from HFE (Fig. 5) and 91 from LCH (Fig. 6). Among those measurements, 125 are from PKS, 50 are from SKKS and 185 are from SKS (Supporting Information Table S1). As shown in Figs 2(a) and (b), most of the SKS events have a BAZ ranging from 100° to 140° and are located in the western Pacific subduction zones. The PKS measurements are mostly from events with a BAZ in the range of 5°–35°, and the SKKS measurements have two main BAZ ranges which are 0°–35° and 300°–360°. Both the PKS and SKKS events are from the west coast of Central and South America (Fig. 2a), and including these non-SKS phases significantly improves the backazimuthal coverage of the SWS measurements. Because a large quantity of well-defined splitting parameters are observed at all the three stations, null measurements, which are characterized by a lack of observable energy on the transverse component, will not be discussed in this study.

3.1 Station ENH

The 191 measurements obtained at Station ENH have a mean δt of 0.67 ± 0.18 s and a mean $\boldsymbol{\phi}$ of 110.8 ± 48.4°, ranging from 0.35 to 1.15 s and 4° to 175°, respectively. The SKS events record by station ENH mostly come from the western Pacific subduction zones in an

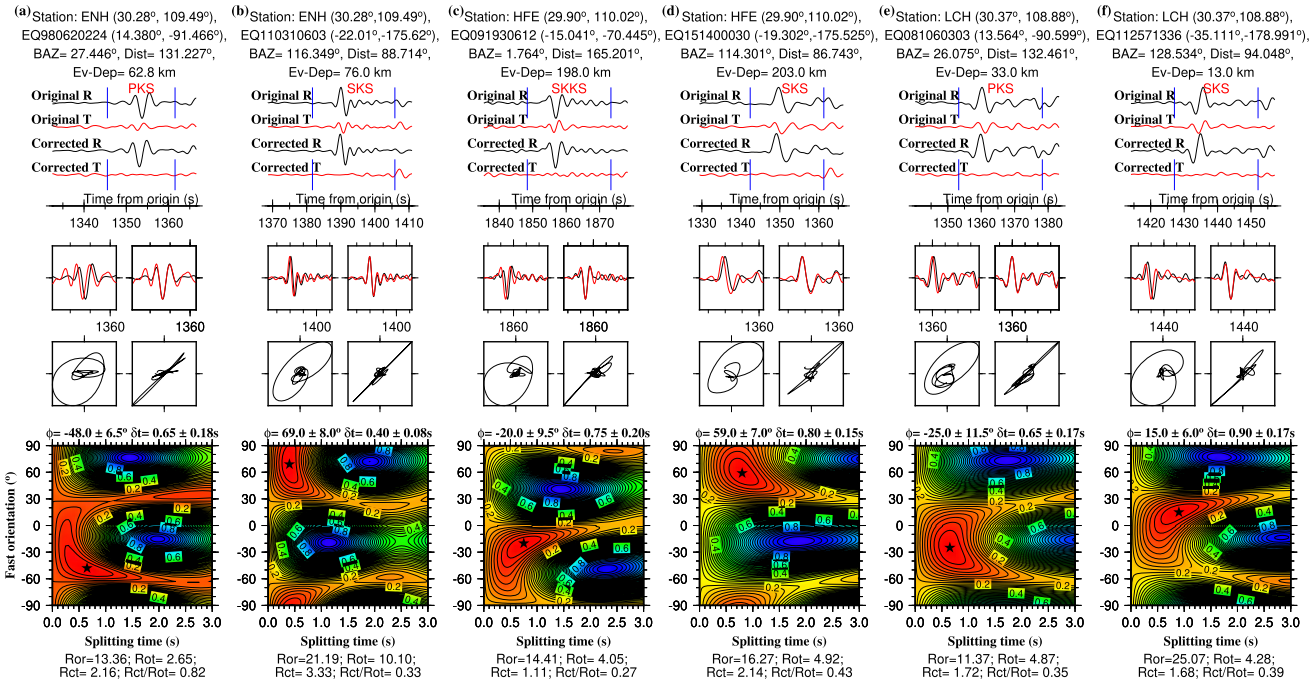

Figure 3. Examples of SWS measurements (quality A) recorded by stations ENH, HFE and LCH. The plots in the top row show original and corrected radial and transverse components, and the plots in the central rows show the uncorrected and corrected particle motions of the fast and slow particles. The bottom plots are misfit maps, with the colour representing the energy on the corrected transverse component. The optimal pair of splitting parameters correspond to the minimum value on the misfit map and are indicated by the star.

approximately 110°–125° BAZ range with dominantly ENE–WSW fast orientations. The PKS and SKKS events are mainly from the west coast of Central and South America in the BAZ ranges of 0–40° and 340–360° with mostly NW-SE fast orientations (Fig. 4). When the fast orientations are plotted in the modulo 90° BAZ domain, two distinct groups of measurements are found in the BAZ (modulo-90°) range of 15–30° (Fig. 4c). Those in the first group are mostly SKS measurements and the fast orientations are in the range of 36–92°, and those in the second group are SKKS or PKS measurements with fast orientations from about 120° to nearly N–S. The apparent azimuthal variation is inconsistent with a multiple layered anisotropic structure which is characterized by a systematic azimuthal variation with a 90° periodicity (Silver & Savage 1994; Rumpker & Silver 1998), that is in a modulo-90° domain, the splitting parameters are expected to have similar values for a given BAZ.

Several studies have measured shear wave splitting at this station, as summarized in Table 1. The number of individual measurements obtained by the studies ranges from 7 to 61 (while this study obtained 191 measurements). Except for Huang *et al.* (2011) which uses SKS, SKKS, PKS and SKiKS, and Liu & Gao (2013) which uses XKS, to our knowledge, all the other studies only use the SKS phase. The station averaged fast orientations for these previous studies (Iidaka & Niu 2001; Luo *et al.* 2004; Wang *et al.* 2013) are between 37° and 77° which is comparable to the value of 61° from this study when only the SKS phase is used and are significantly different from results obtained using PKS and SKKS (about 138°). On the other hand, results from each of the three XKS phases obtained in our study are statistically consistent with the corresponding values reported by Liu & Gao (2013) (Table 1). Those comparisons suggest that only using a single phase could result in misleading results. In addition, station averages are heavily dependent on the relative proportion of the events from the different BAZ groups, and thus do not objectively reflect the true anisotropy characteristics beneath this station.

3.2 Station HFE

The 78 events recorded by Station HFE resulted in a mean δt of 0.93 ± 0.29 s and a mean $\boldsymbol{\phi}$ of 55.9 ± 32.6° (Fig. 5). The PKS and SKKS measurements are mainly from BAZ ranges of 0–15° and 330–360°, and the resulting fast orientations are dominantly NW–SE. In contrast, the SKS measurements are mostly from events in the BAZ range spanning from 110° to 130° and the fast orientations are mostly NE–SW. A group of five measurements from events in the SW quadrant demonstrate mostly E–W fast orientations (Fig. 5i). Similar to ENH, the azimuthal variations are inconsistent with a multiple layered anisotropic structure (Fig. 5c).

Previous studies conducted at this station (Wang *et al.* 2013; Zhao *et al.* 2013; Li *et al.* 2018; Yang *et al.* 2019) all used the SKS phase, and the number of measurements ranges from 1 to 11 comparing to 78 obtained by this study. The fast orientations from the previous studies range from 47° to 86°, while the splitting times are between 0.48 and 1.26 s. Similar to ENH, our SKS fast orientation (52°) is comparable to results from the previous SKS splitting measurements, but significantly different fast orientations with those obtained by previous studies are found when PKS and SKKS are used.

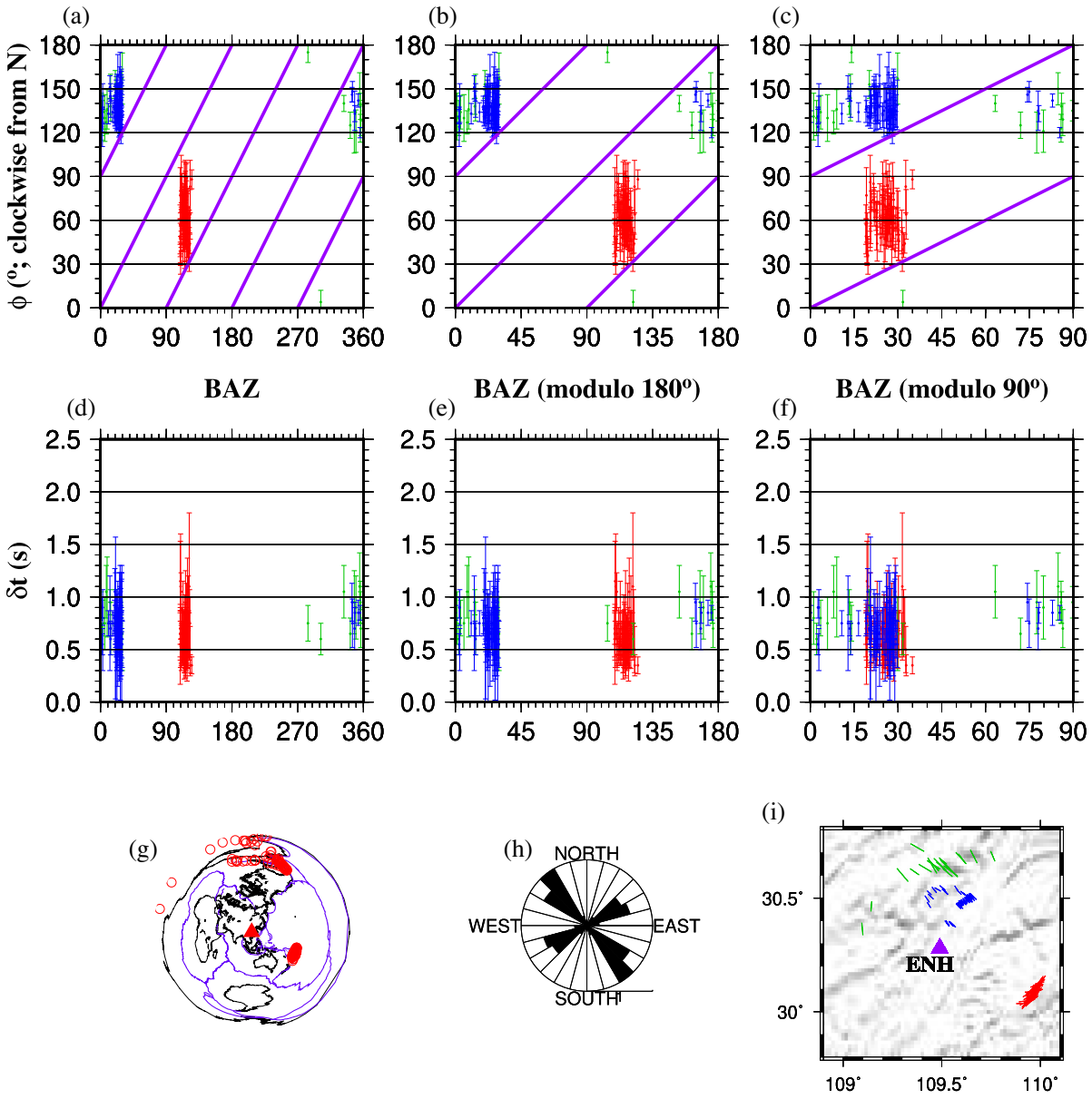

Figure 4. Summary of measurements at Station ENH. (a) Azimuthal variations of the fast orientation plotted against backazimuth. (b) Same as (a) but for the modulo-180° backazimuth. (c) Same as (a) but for the modulo-90° backazimuth. The purple lines in (a)–(c) show $\boldsymbol{\phi} = n*90 + \mathrm{BAZ}$, where $n = -3, -2, -1$, 0 and 1, along which the fast orientation is parallel or orthogonal to the BAZ and thus well-defined measurements are non-existent for simple anisotropy. (d–f) Same as (a)–(c) but for splitting times; (g) an azimuthal equidistant projection map showing events used (circles); (h) a rose diagram showing the distribution of the measured fast orientations; (i) splitting parameters plotted above ray-piercing points at 200 km depth. The triangle represents the station. For all the plots, red, green and blue colours represent the SKS, SKKS and PKS measurements, respectively.

3.3 Station LCH

The 91 pairs of measurements from LCH have dominantly N–S fast orientations with a mean value of 178.2 ± 17.0°, and the resulting δt values range from 0.4 to 1.4 s with a mean of 0.78 ± 0.18 s. The measurements can be divided into two groups based on the BAZ range of the events. The first group, which is mostly composed of SKKS and PKS measurements, has a BAZ in the range of 15–40°, and the second group, which are mostly SKS measurements, has a BAZ range between 120° and 140° (Fig. 6). For the first group, the mean splitting parameters are 167.3 ± 11.6° for the fast orientation, and 0.85 ± 0.16 s for the splitting time, and for the second group, the corresponding values are 12.8 ± 10.3° and 0.69 ± 0.16 s.

Only one previous study measured SWS at this station (Zhao *et al.* 2011), which reported a fast orientation of 128° and a splitting time of 2.54 s from a single SKS event. Both the fast orientation and the splitting time are significantly different from results obtained by this study using any of the three phases (Table 1).

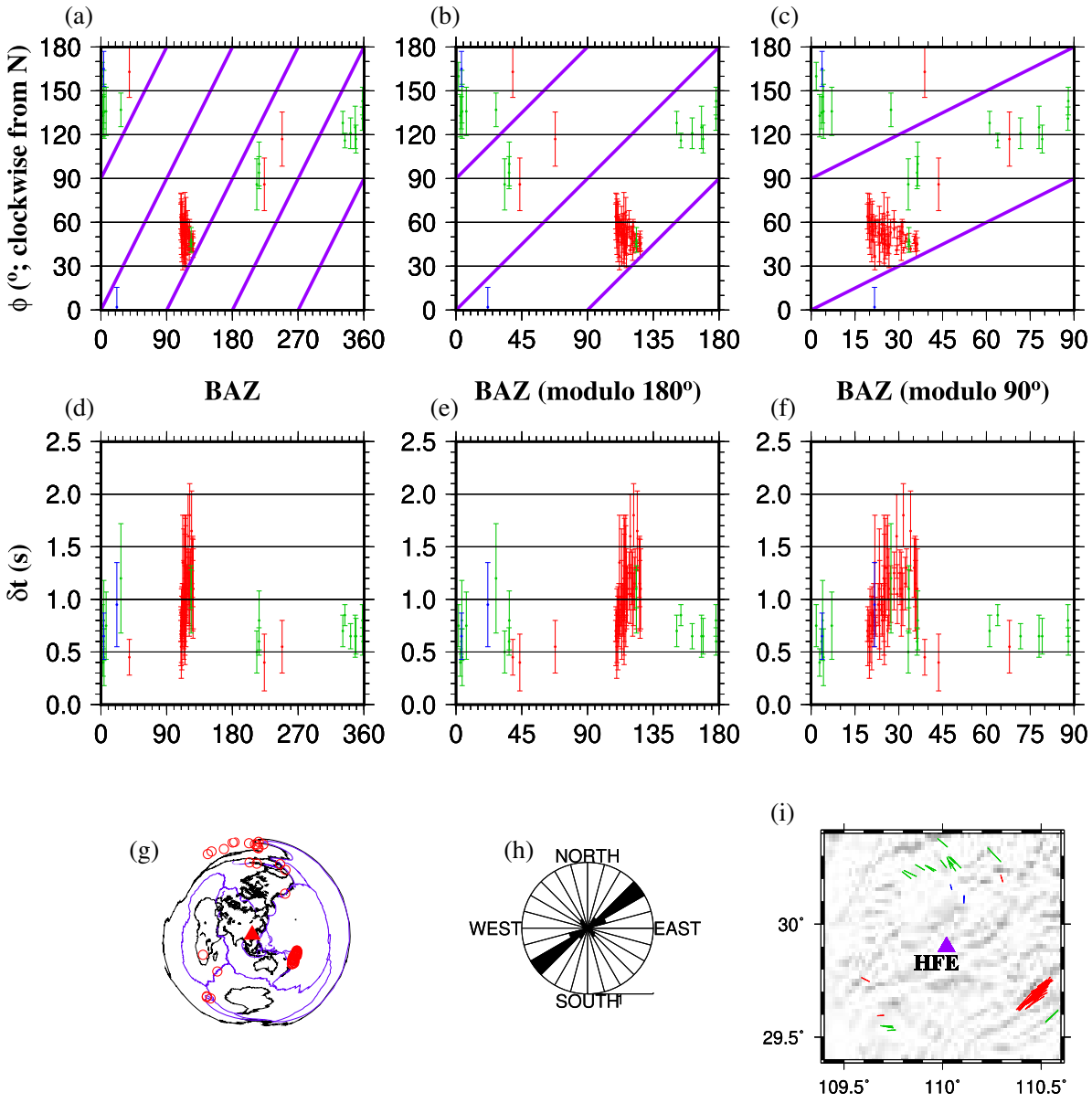

Figure 5. Same as Fig. 4 but for Station HFE.

4 DISCUSSION

4.1 Evidence for piercing-point-dependent anisotropy

The clear dependence of the splitting parameters on the arriving azimuth of the XKS events adequately indicates that the observed splitting parameters cannot be readily explained by a laterally homogenous single layer of anisotropy with a horizontal axis of symmetry, which is an assumption when the vast majority of previous SWS studies employed for interpreting the measurements. Traditionally, departures from this ideal model are termed as complex anisotropy (Silver & Savage 1994), and the most commonly observed complex anisotropy is composed of two or more layers with horizontal but non-parallel and non-orthogonal axes of symmetry. These multiple layers of anisotropy are characterized by a systematic azimuthal variation of both the $\boldsymbol{\phi}$ and δt observations, typically possessing a 90° periodicity (Rumpker & Silver 1998), which is not observed at any of the three stations (Figs 4–6). Additionally, for multiple layered anisotropy, some of the $\boldsymbol{\phi}$ values can be approximately parallel or orthogonal to the BAZ (Liu & Gao 2013), which are also not observed (Figs 4–6). Therefore, the observed apparent azimuthal variations of the splitting parameters cannot be reliably attributed to multilayered anisotropy.

Relative to two-layered anisotropy, a less commonly observed form of complex anisotropy is constituted by a single layer with a dipping axis of symmetry (Levin & Park 1997; Levin *et al.* 2007), which is characterized by a systematic azimuthal variation of the splitting parameters with a 180° periodicity. Even though the azimuthal distribution of the XKS events is limited at some of the stations, it is clear that a 180° periodicity is absent at all the three stations (Figs 4b, 5b and 6b). Compared with multilayered or dipping axis models, a more viable scenario

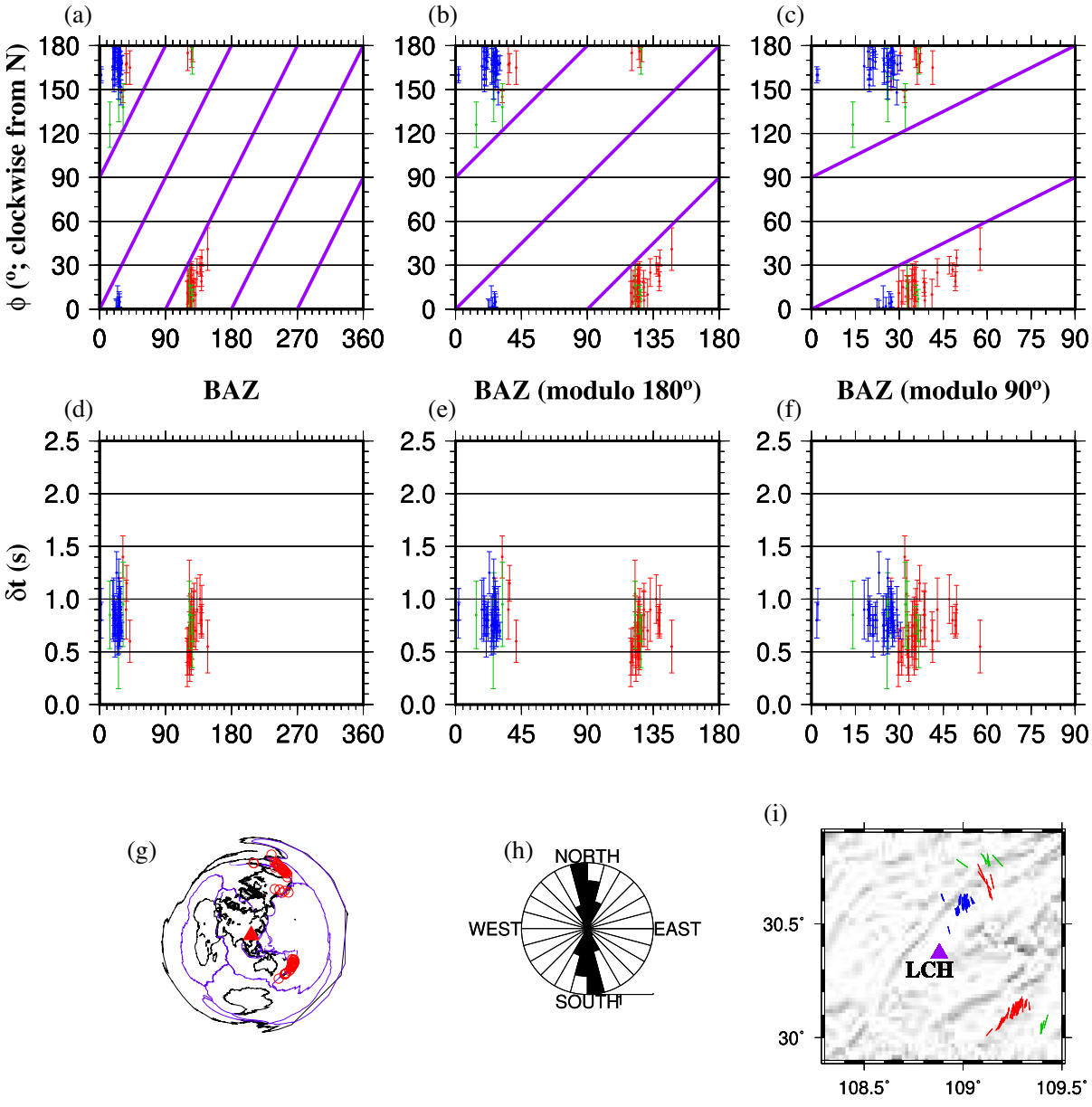

Figure 6. Same as Fig. 4 but for Station LCH.

is spatially varying simple anisotropy. In addition to the lack of 90° or 180° periodicity, the strongest evidence for this model is from the fact that when the observed splitting parameters are projected at a certain depth, a spatially coherent pattern is observed, as detailed in the next section.

4.2 Anisotropy depth estimation

We next project the splitting measurements to different depths and explore the spatial consistency of the splitting parameters. With increasing depth, the piercing points of the XKS rays recorded by the stations spread away from the stations and eventually overlap (Fig. 7). As the assumed depth approaches ∼250 km, measurements with nearby piercing points show the highest similarity to each other (Fig. 7e) and can be approximately divided into three groups. Those in the group north of 30.2° N latitude have a dominantly NW-SE fast orientation, those in the south-central part of the study area are mostly E–W oriented, and the rest measurements have mostly NE–SW fast orientations. The spatial coherency appears to decrease at greater depth (Fig. 7f).

We use two approaches, which are identical in principle but different in visual display and vertical sampling intervals, to quantify the initial observation that the spatial coherency of the splitting parameters vary with the assumed depth, and to locate the optimal depth with the highest spatial coherency. For the first approach, we divide the study area into overlapping circles with a 0.2° radius and 0.2° distance between the neighbouring circles. For each depth, we calculate the sample standard deviation (SD) of the fast orientations within each of the

Table 1. *SWS* measurements from previous and the present studies.

Station	Phase	ϕ (°)	σ_ϕ (°)	δt (s)	$\sigma_{\delta t}$ (s)	N	Reference
ENH	SKS	75.6	7.4	0.36	0.13	7	Iidaka & Niu (2001)
	SKS	63.0	14.6	0.60	0.01	12	Luo *et al.* (2004)
	SKS	37.0	-	1.05	-	10	Zhao *et al.* (2007)
	XKS	155.7	52.0	0.73	0.40	10	Huang *et al.* (2011)
	SKS	77.2	4.8	0.45	0.01	22	Wang *et al.* (2013)
	XKS	104.3	49.3	0.71	0.20	61	Liu & Gao (2013)
	SKS	61.0	11.0	0.61	0.17	28	Liu & Gao (2013)
	SKKS	143.9	26.9	0.88	0.21	11	Liu & Gao (2013)
	PKS	134.2	4.1	0.75	0.18	22	Liu & Gao (2013)
	XKS	110.8	48.4	0.67	0.18	191	This study
	SKS	61.4	13.0	0.60	0.17	88	This study
	SKKS	137.8	16.1	0.84	0.16	21	This study
	PKS	137.5	7.1	0.70	0.14	82	This study
HFE	SKS	67.3	2.1	1.03	0.10	7	Wang *et al.* (2013)
	SKS	47.2	8.6	1.26	0.13	11	Zhao *et al.* (2013)
	SKS	83.7	-	0.48	-	1	Li *et al.* (2018)
	SKS	85.5	-	0.50	-	1	Yang *et al.* (2019)
	XKS	55.9	32.6	0.93	0.29	78	This study
	SKS	52.4	13.2	1.00	0.28	57	This study
	SKKS	125.4	27.7	0.73	0.21	19	This study
	PKS	173.5	8.6	0.80	0.21	2	This study
LCH	SKS	128.0	-	2.54	-	1	Zhao *et al.* (2011)
	XKS	178.2	17.0	0.78	0.18	91	This study
	SKS	9.7	14.9	0.73	0.21	40	This study
	SKKS	167.8	23.6	0.78	0.12	10	This study
	PKS	169.9	8.7	0.83	0.13	41	This study

circles and then get the average of SD value for each of the depths of 0, 100, 150, 200, 250, 300 and 350 km. A circle is not employed if the number of splitting measurements in it is one or less. The results show that the lowest averaged SD value is found at 250 km (Fig. 8e). For the second approach, we apply the spatial coherency method first proposed in Gao *et al.* (2010). This technique employs the idea that the observed splitting parameters will reach the highest spatial coherency if the assumed anisotropy depth is correct (see Liu & Gao 2011; Gao & Liu 2012 for the detailed descriptions). The conditions for the technique to be reliably applied, including adequate BAZ coverage, densely spaced (e.g. 70 km or less) stations, and spatially varying simple anisotropy, can all be satisfied in this study area. The resulting F_v, which is a dimensionless factor reflecting the spatial variation of the measurements as a function of the assumed depth of anisotropy, shows a clear minimum at the depth of 250 km (Fig. 8h), a conclusion that is consistent with results from the previous approach. The actual thickness of the anisotropic layer is dependent on the anisotropy amplitude. Under the assumption that the layer has a mean anisotropy of 4 per cent (Mainprice & Silver 1993), a splitting time of 0.75 s corresponds to a thickness of ∼80 km.

4.3 Synthetic test

Like it is routinely assumed by the vast majority of SWS studies, the above analysis and interpretation of the SWS measurements were made based on the ray theory, that is the measurements only reflect physical properties along the geometric ray paths. In reality, due to the finite frequencies of the XKS waves, the splitting measurements are functions of anisotropy primarily in the first Fresnel zone (Alsina & Snieder 1995; Chevrot 2006). For a shear wave with a dominant frequency of 0.15 Hz, the radius of the first Fresnel zone at 250 km depth is about 60 km. As shown in Figs 2(a) and (b), most of the events used in the study are from either the north or the southeast. For a given station, the Fresnel zones of the XKS waves from the two groups overlap significantly at shallow depth (e.g. $<$ 100 km), and the amount of overlapping decreases at greater depths (see Fig. 9b for an example for Station ENH). At the optimal depth of 250 km, the overlapping area is merely 13 per cent of the area of the first Fresnel zone, suggesting that at this (and greater) depth, the two groups of events recorded by the same station sample different regions.

To test if a sharp E–W boundary separating the two regions of anisotropy can indeed produce the observed pattern of splitting parameters, we used the SPECFEM3D_GLOBE package (Komatitsch & Vilotte 1998; Komatitsch & Tromp 1999) to produce synthetic seismograms. Ideally, given the large (∼83°–180°) epicentral distances for the XKS waves, a global-scale simulation with a realistic 3-D structure should be used for simulating wave propagation. However, in order to achieve frequencies that are high enough to match those of the XKS waves,

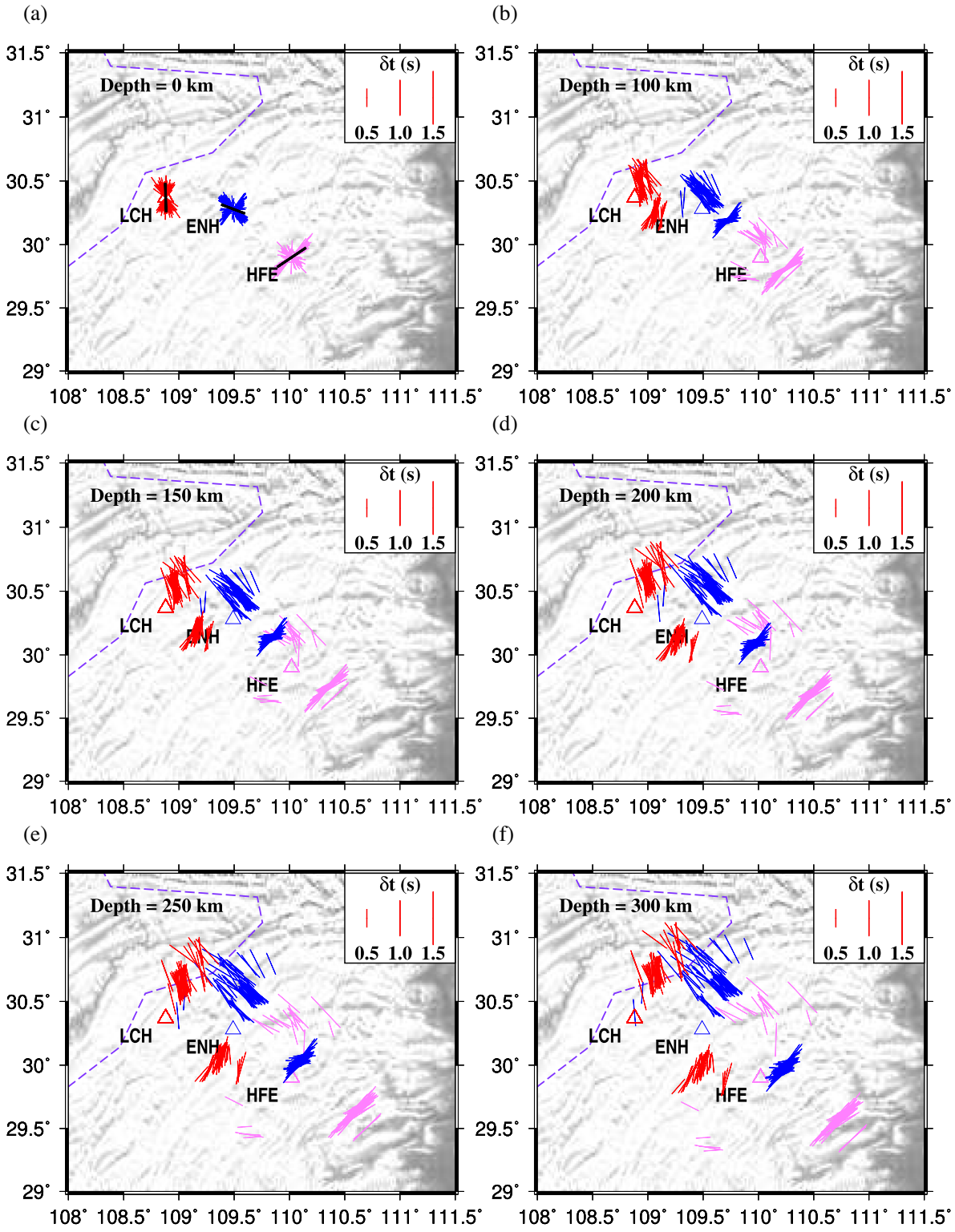

Figure 7. PKS, SKKS and SKS splitting parameters (qualities A and B) from this study plotted at piercing-point locations at different depths. The depth values are shown in the upper left corner. The black bars in (a) are the station averaged SWS parameters, and the red, blue and pink bars indicate individual measurements from stations LCH, ENH and HFE, respectively.

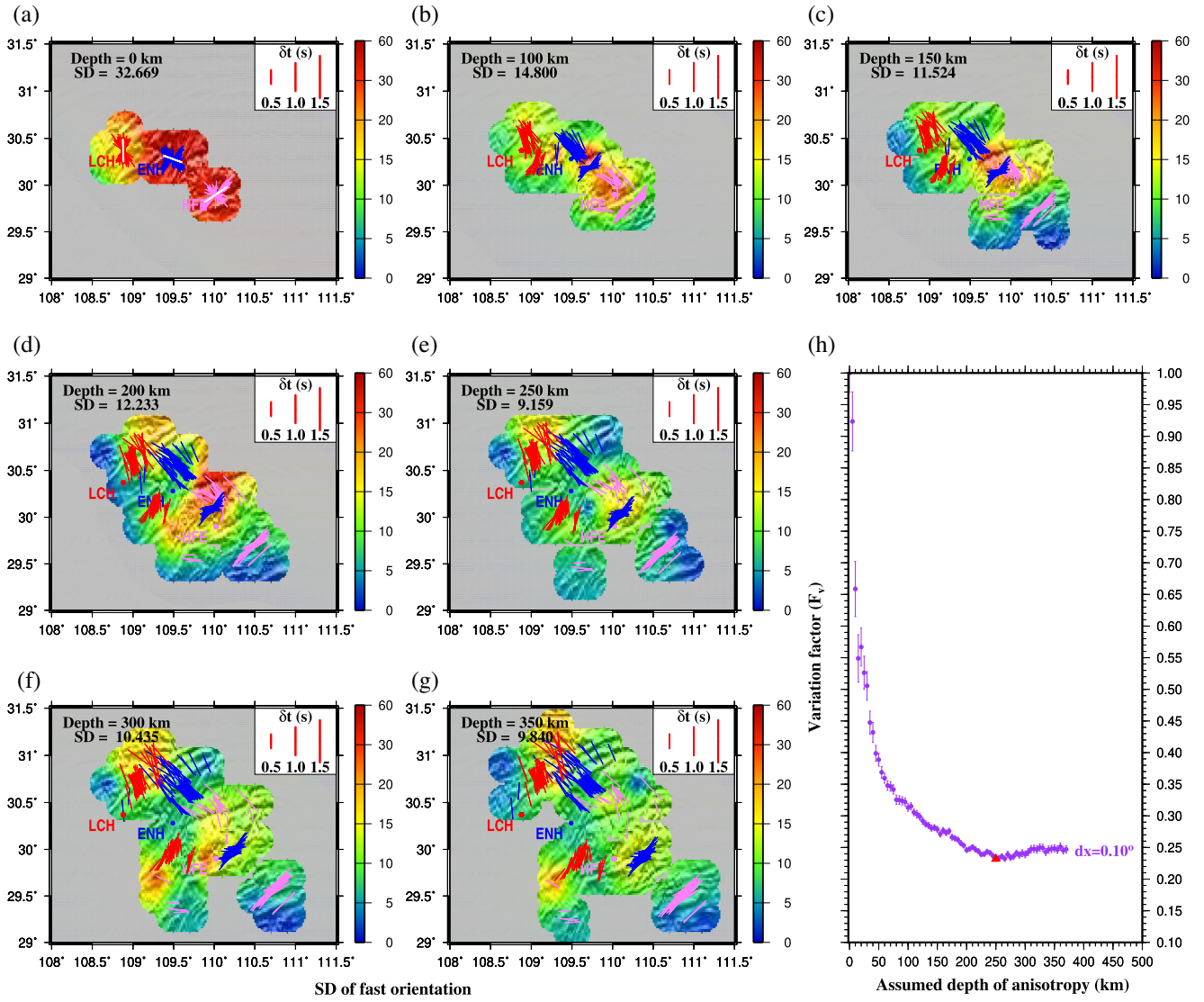

Figure 8. (a–g) Distribution of the standard deviation (SD) of spatially averaged fast orientations in 0.2° radius circles at the depths of 0, 100, 150, 200, 250, 300 and 350 km. The averaged SD results are indicated in the upper left corner of each map. The results plotted were resampled into a resolution of 0.1°. The red, blue and pink bars indicate individual measurements of stations LCH, ENH and HFE, respectively. (h) Anisotropy depth analysis for the SWS measurements based on the spatial coherence technique (Liu & Gao 2011), resulting in an optimal depth of anisotropy at 250 km. The red triangle on the curve marks the depth with the minimum variation factor.

the computational cost for a global scale simulation is unrealistically high at the present time, and is actually not essential for our purpose, as demonstrated below.

We constructed a regional model with a depth range of 0–950 km and a surface area of 10° by 10° centred at station ENH. The model has 256 surface spectral elements and is capable of producing synthetic seismograms for periods longer than ∼1.9 s which is comparable to the dominant period of the XKS waves used in the study. The transversely isotropic version of the spherically symmetric Preliminary Reference Earth Model (PREM; Dziewonski & Anderson 1981) was used as the background model, and an azimuthally anisotropic layer at the depth range of 200–280 km was introduced based on the estimated optimal depth and layer thickness. The fast orientation and splitting time of the layer for the area north of Station ENH were set as −30° and 0.8 s, respectively, and those in the area south of the station were set as 60° and 0.8 s, respectively. For each of the three stations, an event from the northern group and another event from the SE group were chosen for the simulation. Because the source must reside inside the volume, a local event was placed at the piercing point of the corresponding XKS ray path at 500 km depth. As the initial polarization orientation of the shear wave from a local event is dependent on the focal mechanism, the technique of minimizing the lesser of the two eigenvalues of the covariance matrix of the seismograms (Silver & Chan 1991) is used to simultaneously search for the initial polarization and the splitting parameters. Fig. 10 shows example synthetic seismograms and their splitting analyses. A comparison of the resulting splitting parameters computed from the synthetic and observed seismograms (Fig. 9 and Supporting Information Table S2) suggests a simple model with two uniform regions of anisotropy and a sharp vertical boundary can explain the major characteristics of the SWS measurements reasonably well.

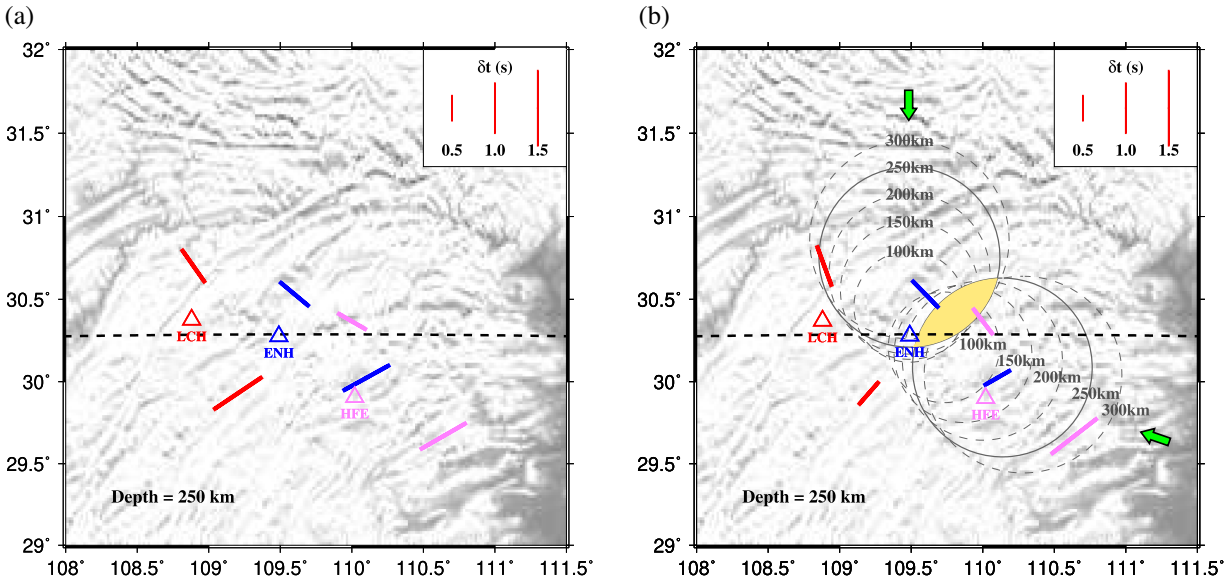

Figure 9. Comparison of SWS measurements using synthetic seismograms generated using SPECFEM3D_GLOBE (a) and those from corresponding observed seismograms (b). For each station (triangles), the splitting parameters (bars) from an event from north and another event from southeast are measured and are plotted at the 250 km depth piercing points using the same colour as the station. The circles in (b) are the first Fresnel zones from two events (whose backazimuths are marked by the green arrows) recorded by Station ENH at various depths. The solid circles are the Fresnel zones at 250 km depth. The E–W dashed line approximately separates two regions of anisotropy with different fast orientations.

4.4 Geodynamic implications

Previous studies suggest that the lithospheric thickness beneath the study area is between ∼200 and 250 km (Wang *et al.* 2013; Pasyanos *et al.* 2014; Shan *et al.* 2021), which is comparable to the ∼250 km resultant optimal depth of anisotropy (Fig. 8h). We thus speculate that the anisotropy observed beneath the three stations mainly comes from the upper asthenosphere, in the rheological transition zone between the lithosphere and the asthenosphere. This conclusion is consistent with the result of numerous previous seismic anisotropy studies proposing that mantle flow plays an important role in the formation of seismic anisotropy beneath central China and its adjacent areas (e.g. Bai *et al.* 2009; Huang *et al.* 2011, 2015; Li *et al.* 2011; Kong *et al.* 2018), probably from the westward subduction of the Pacific plate, mantle flow associated with absolute plate motion (APM) of the Eurasian Plate (e.g. Huang *et al.* 2011) or with India–Eurasia collision (e.g. Bai *et al.* 2009; Li *et al.* 2011; Huang *et al.* 2015; Kong *et al.* 2018; Liu *et al.* 2019).

The bottom of the thick lithosphere of the Sichuan Basin (SCB) is revealed to have a downward cone shape by some previous seismic tomographic studies (e.g. Pasyanos *et al.* 2014; Bao *et al.* 2015; Van der Meer *et al.* 2018; Shan *et al.* 2021). The SWS measurements we obtained in this study have two dominant fast orientations and are spatial clustered when they are projected to the optimal depth of 250 km, approximately separated by the latitude of station ENH (Fig. 8e). The fast orientations in the northern group are approximately consistent with the APM direction, and those in the southern group are subparallel to the strike of the margin of the lithospheric root of the SCB in the area (NE–SW). These observations can be explained by a simple mantle flow model that consists of both APM-induced and root-deflected mantle flow systems (Fig. 11), similar to what has been proposed for other areas with large lateral variations in lithospheric thickness such as the southern and eastern edges of the North American craton (Fouch *et al.* 2000; Refayee *et al.* 2014; Yang *et al.* 2014, 2017). Under this model, the NW–SE fast orientations in the northern area reflect APM-induced anisotropy or a combination of APM-induced anisotropy and anisotropy associated with a flow field moving around the northern edge of the thick lithospheric block, while the NE–SW oriented anisotropy observed in the southern area, which is inconsistent with the APM direction, is associated with the flow system deflected by the eastern edge of the thick lithospheric block beneath the SCB. The proposed model provides a viable explanation for the puzzling observation that around the NE corner of the SCB, the fast orientations are different from those observed in the surrounding areas (Fig. 1). This model can also explain most previous SWS measurements in the vicinity of the SCB, especially those in its peripheral areas (Fig. 11). The general agreement between the observed fast orientations and those predicted by the mantle flow system inferred from the model implies that to the first order, lithospheric fabric has a less significant contribution than mantle flow to the observed azimuthal anisotropy in the vicinity of the SCB, although a more quantitative evaluation of the contribution from each of the layers cannot be made solely based on SWS measurements presented in this study. The dominantly sublithospheric origin of the observed anisotropy is also hinted by the estimated depth of the source of anisotropy based on the spatial coherency analysis, and the fact that events from different azimuthal recorded by the same station show different splitting parameters (Alsina & Snieder 1995).

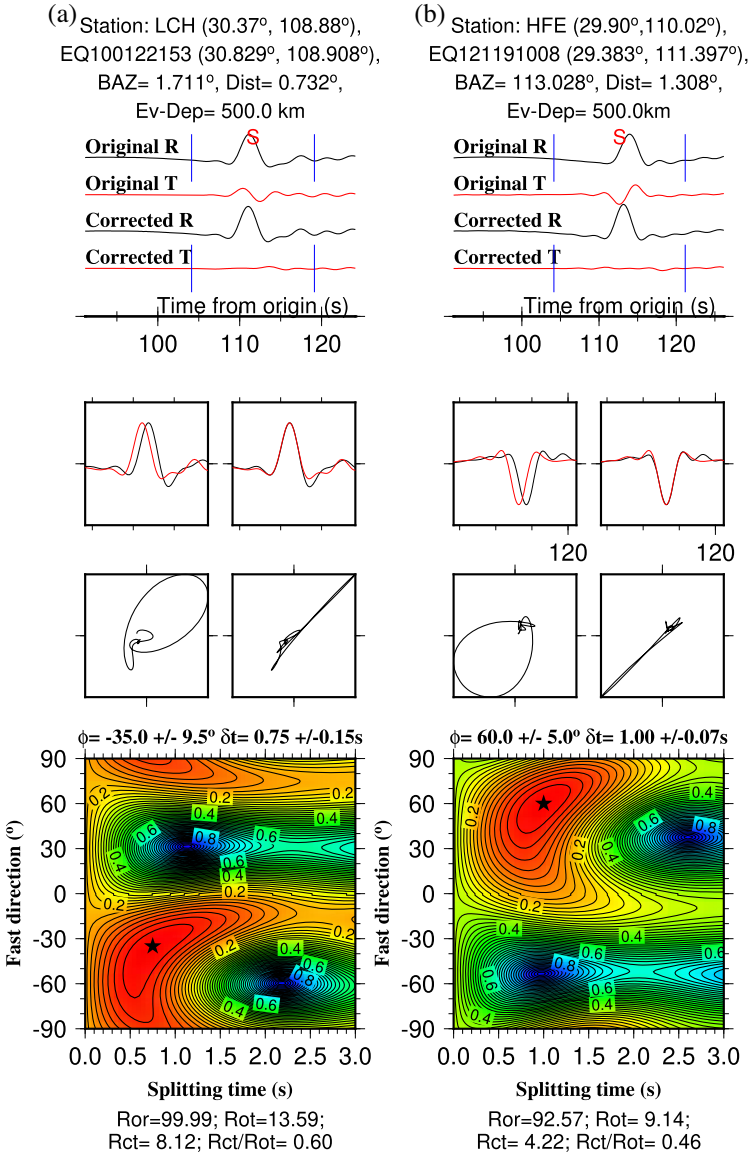

Figure 10. Same as Fig. 3 but for the SWS measurements computed from the synthetic seismograms for two station–event pairs.

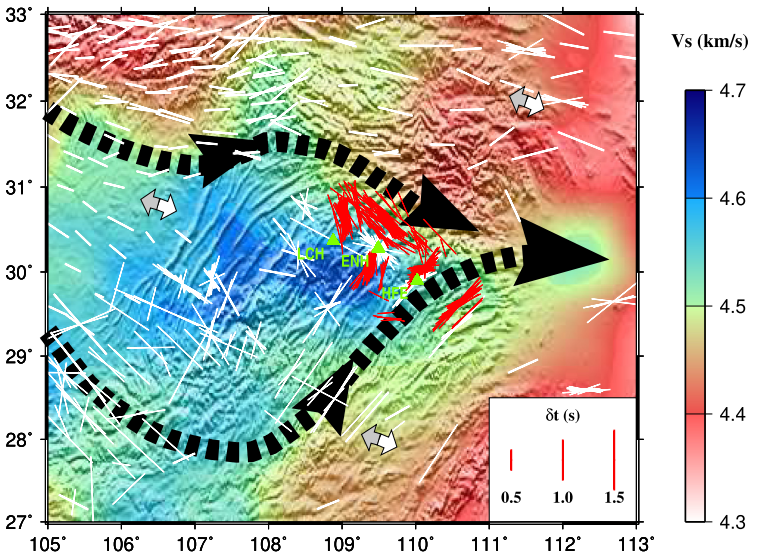

Figure 11. A schematic model showing the mantle flow field beneath the SCB and adjacent areas. The white and red bars are SWS measurements from previous studies and this study, respectively. The black dashed lines with arrows indicate the direction of mantle flow deflected by the keel of the thick lithosphere beneath the SCB. The background colour denotes shear wave velocities at the depth of 160 km (Bao *et al.* 2015). The grey and white arrows represent the APM directions computed using the HS3-NUVEL-1A model (Gripp & Gordon 2002) and the NNR-MORVEL56 model (Argus *et al.* 2011), respectively.

5 CONCLUSIONS

The SWS measurements observed at three stations situated near the NE margin of the SCB exhibit systematic azimuthal variations in the fast orientations and lack a 90° or 180° periodicity which is expected for the most common forms of complex anisotropy. Spatial coherency analysis of the splitting parameters suggests that the source of anisotropy beneath the study area mostly locates in the depth of ∼250 km which is comparable to the depth of the bottom of the seismically determined lithosphere in the area. The observations can be explained by a simple geodynamic model invoking APM-related simple shear in the transitional layer between the partially coupled lithosphere and the asthenosphere, and mantle flow deflected by the thick lithospheric root of the SCB in the upper asthenosphere. This study advocates the consideration of laterally heterogeneous anisotropy structures for the interpretation of splitting measurements.

ACKNOWLEDGEMENTS

We thank S. Chevrot, an anonymous reviewer, and the editor I. Bastow for their constructive reviews that significantly improved the manuscript, and X. Bao for providing the velocity model plotted in Fig. 11. All the figures were produced using the Generic Mapping Tools (Wessel *et al.* 2019). This study was partially supported by the U.S. National Science Foundation under awards 1830644 to KL and SG and 1919789 to SG.

DATA AVAILABILITY

Data used in the study are available from the IRIS DMC (http://ds.iris.edu/ds/nodes/dmc; last accessed: December 2019) and Data Management Centre of China National Seismic Network at Institute of Geophysics, China Earthquake Administration (SEISDMC; last accessed: September 2019).

REFERENCES

Alsina, D. & Snieder, R., 1995. Small-scale sublithospheric continental mantle deformation: constraints from SKS splitting observations, *Geophys. J. Int.,* **123,** 431–448.

Ando, M., Ishikawa, Y. & Wada, H., 1980. S-wave anisotropy in the upper mantle under a volcanic area in Japan, *Nature,* **286,** 43–46.

Ando, M., Ishikawa, Y. & Yamazaki, F., 1983. Shear wave polarization anisotropy in the upper mantle beneath Honshu, Japan, *J. geophys. Res.,* **88**(B7), 5850–5864.

Argus, D.F., Gordon, R.G. & DeMets, C., 2011. Geologically current motion of 56 plates relative to the no-net-rotation reference frame, *Geochem. Geophys. Geosyst.,* **12**(11), doi:10.1029/2011gc003751.

Bai, L., Iidaka, T., Kawakatsu, H., Morita, Y. & Dzung, N., 2009. Upper mantle anisotropy beneath Indochina block and adjacent regions from shear-wave splitting analysis of Vietnam broadband seismograph array data, *Phys. Earth planet. Inter.,* **176**(1–2), 33–43.

Bao, X., Song, X. & Li, J., 2015. High-resolution lithospheric structure beneath Mainland China from ambient noise and earthquake surface-wave tomography, *Earth planet. Sci. Lett.,* **417,** 132–141.

Ben Ismail, W. & Mainprice, D., 1998. An olivine fabric database: an overview of upper mantle fabrics and seismic anisotropy, *Tectonophysics,* **296,** 145–157.

Chevrot, S., 2006. Finite-frequency vectorial tomography: a new method for high-resolution imaging of upper mantle anisotropy, *Geophys. J. Int.,* **165,** 641–657.

Dziewonski, A.M. & Anderson, D.L., 1981. Preliminary reference Earth model, *Phys. Earth planet. Inter.,* **25**(4), 297–356.

Fouch, M.J. & Rondenay, S., 2006. Seismic anisotropy beneath stable continental interiors, *Phys. Earth planet. Inter.,* **158**(2–4), 292–320.

Fouch, M.J., Fischer, K.M., Parmentier, E.M., Wysession, M.E. & Clarke, T.J., 2000. Shear wave splitting, continental keels, and patterns of mantle flow, *J. geophys. Res.,* **105**(B3), 6255–6275.

Francis, T.J.G., 1969. Generation of seismic anisotropy in the upper mantle along the mid-oceanic ridges, *Nature,* **221**(5176), 162–165.

Fuchs, K., 1977. Seismic anisotropy of the subcrustal lithosphere as evidence for dynamical processes in the upper mantle, *Geophys. J. Int.,* **49**(1), 167–179.

Gao, S.S. & Liu, K.H., 2012. AnisDep: a FORTRAN program for the estimation of the depth of anisotropy using spatial coherency of shear-wave splitting parameters, *Comput. Geosci.,* **49,** 330–333.

Gao, S., Davis, P.M., Liu, H., Slack, P.D., Zorin, Y.A., Mordvinova, V.V., Kozhevnikov, V.M. & Meyer, R.P., 1994. Seismic anisotropy and mantle flow beneath the Baikal rift zone, *Nature,* **371**(6493), 149–151.

Gao, S.S., Liu, K.H., Stern, R.J., Keller, G.R., Hogan, J.P., Pulliam, J. & Anthony, E.Y., 2008. Characteristics of mantle fabrics beneath the south-central United States: constraints from shear-wave splitting measurements, *Geosphere,* **4,** 411–417.

Gao, S.S., Liu, K.H. & Abdelsalam, M.G., 2010. Seismic anisotropy beneath the Afar Depression and adjacent areas: implications for mantle flow, *J. geophys. Res.,* **115**(B12), doi:10.1029/2009jb007141.

Gripp, A.E. & Gordon, R.G., 2002. Young tracks of hotspots and current plate velocities, *Geophys. J. Int.,* **150,** 321–361.

Hess, H.H., 1964. Seismic anisotropy of the uppermost mantle under oceans, *Nature,* **203**(4945), 629–631.

Huang, Z., Wang, L., Zhao, D., Mi, N. & Xu, M., 2011. Seismic anisotropy and mantle dynamics beneath China, *Earth planet. Sci. Lett.,* **306**(1–2), 105–117.

Huang, Z. *et al.*, 2015. Teleseismic shear-wave splitting in SE Tibet: insight into complex crust and upper-mantle deformation, *Earth planet. Sci. Lett.,* **432,** 354–362.

Iidaka, T. & Niu, F., 2001. Mantle and crust anisotropy in the eastern China region inferred from waveform splitting of SKS and PpSms, *Earth Planets Space,* **53**(3), 159–168.

Kennett, B.L.N. & Engdahl, E.R., 1991. Traveltimes for global earthquake location and phase identification, *Geophys. J. Int.,* **105**(2), 429–465.

Komatitsch, D. & Vilotte, J.P., 1998. The spectral-element method: an efficient tool to simulate the seismic response of 2D and 3D geological structures, *Bull. seism. Soc. Am.,* **88,** 368–392.

Komatitsch, D. & Tromp, J., 1999. Introduction to the spectral element method for three-dimensional seismic wave propagation, *Geophys. J. Int.,* **139**(3), 806–822.

Kong, F., Wu, J., Liu, L., Liu, K.H., Song, J., Li, J. & Gao, S.S., 2018. Azimuthal anisotropy and mantle flow underneath the southeastern Tibetan Plateau and northern Indochina Peninsula revealed by shear wave splitting analyses, *Tectonophysics,* **747,** 68–78.

Leven, J.H., Jackson, I. & Ringwood, A.E., 1981. Upper mantle seismic anisotropy and lithospheric decoupling, *Nature,* **289**(5795), 234–239.

Levin, V. & Park, J., 1997. Crustal anisotropy in the Ural Mountains Foredeep from teleseismic receiver functions, *Geophys. Res. Lett.,* **24**(11), 1283–1286.

Levin, V., Okaya, D. & Park, J., 2007. Shear wave birefringence in wedge-shaped anisotropic regions, *Geophys. J. Int.,* **168**(1), 275–286.

Li, H. *et al.*, 2018. Seismic imaging of lithosphere structure and upper mantle deformation beneath east-central China and their tectonic implications, *J. geophys. Res.,***123**(4), 2856–2870.

Li, Y., Wu, Q., Zhang, F., Feng, Q. & Zhang, R., 2011. Seismic anisotropy of the Northeastern Tibetan Plateau from shear wave splitting analysis, *Earth planet. Sci. Lett.,* **304**(1–2), 147–157.

Liu, K.H. & Gao, S.S., 2011. Estimation of the depth of anisotropy using spatial coherency of shear-wave splitting parameters, *Bull. seism. Soc. Am.,* **101**(5), 2153–2161.

Liu, K.H. & Gao, S.S., 2013. Making reliable shear-wave splitting measurements, *Bull. seism. Soc. Am.,* **103**(5), 2680–2693.

Liu, K.H., Gao, S.S., Gao, Y. & Wu, J., 2008. Shear wave splitting and mantle flow associated with the deflected Pacific slab beneath northeast Asia, *J. geophys. Res.,* **113**(B1), doi:10.1029/2007jb005178.

Liu, L., Gao, S.S., Liu, K.H., Li, S., Tong, S. & Kong, F., 2019. Toroidal mantle flow induced by slab subduction and rollback beneath the Eastern Himalayan syntaxis and adjacent areas, *Geophys. Res. Lett.,* **46,** 11 080–11 090.

Long, M.D. & Silver, P.G., 2008. The subduction zone flow field from seismic anisotropy: a global view, *Science,* **319**(5861), 315–318.

Long, M.D. & Silver, P.G., 2009. Shear wave splitting and mantle anisotropy: measurements, interpretation, and new directions, *Surv. Geophys.,* **30,** 407–461.

Luo, Y., Huang, Z.-X., Peng, Y.-J. & Zheng, Y.-J., 2004. A study on SKS wave splitting beneath the China Mainland and adjacent regions, *Chin. J. Geophys.,* **47**(5), 916–926

Mainprice, D. & Nicolas, A., 1989. Development of shape and lattice preferred orientations: application to the seismic anisotropy of the lower crust, *J. Struct. Geol.,* **11**(1–2), 175–189.

Mainprice, D. & Silver, P.G., 1993. Interpretation of SKS-waves using samples from the subcontinental lithosphere, *Phys. Earth planet. Inter.,* **78,** 257–280.

Mardia, K.V. & Jupp, P.E., 2000. *Directional Statistics,* Wiley, 429p.

Ohuchi, T. & Irifune, T., 2013. Development of A-type olivine fabric in water-rich deep upper mantle, *Earth planet. Sci. Lett.,* **362,** 20–30.

Pasyanos, M.E., Masters, T.G., Laske, G. & Ma, Z., 2014. LITHO1.0: an updated crust and lithospheric model of the Earth, *J. geophys. Res.,* **119**(3), 2153–2173.

Refayee, H.A., Yang, B.B., Liu, K.H. & Gao, S.S., 2014. Mantle flow and lithosphere–asthenosphere coupling beneath the southwestern edge of the North American craton: constraints from shear-wave splitting measurements, *Earth planet. Sci. Lett.,* **402,** 209–220.

Rümpker, G. & Silver, P.G., 1998. Apparent shear-wave splitting parameters in the presence of vertically varying anisotropy, *Geophys. J. Int.,* **135**(3), 790–800.

Savage, M.K., 1999. Seismic anisotropy and mantle deformation: what have we learned from shear wave splitting?, *Rev. Geophys.,* **37**(1), 65–106.

Shan, B., Zhou, W. & Xiao, Y., 2021. Lithospheric thermal and compositional structure of South China jointly inverted from multiple geophysical observations, *Sci. China Earth Sci.,* **64**(1), 148–160.

Silver, P.G., 1996. Seismic anisotropy beneath the continents: probing the depths of geology, *Annu. Rev. Earth Planet. Sci.,* **24**(1), 385–432.

Silver, P.G. & Chan, W.W., 1991. Shear wave splitting and subcontinental mantle deformation, *J. geophys. Res.,* **96**(B10), 16429–16454, doi:10.1029/91jb00899.

Silver, P.G. & Savage, M.K., 1994. The interpretation of shear-wave splitting parameters in the presence of two anisotropic layers, *Geophys. J. Int.,* **119**(3), 949–963.

Van der Meer, D.G., Hinsbergen, D.J.V. & Spakman, W., 2018. Atlas of the underworld: slab remnants in the mantle, their sinking history, and a new outlook on lower mantle viscosity, *Tectonophysics,* **723,** 309–448.

Vinnik, L.P., Makeyeva, L.I., Milev, A. & Usenko, A.Y., 1992. Global patterns of azimuthal anisotropy and deformations in the continental mantle, *Geophys. J. Int.,* **111**(3), 433–447.

Wang, C.Y., Flesch, L.M., Chang, L. & Zheng, T., 2013. Evidence of active mantle flow beneath South China, *Geophys. Res. Lett.,* **40**(19), 5137–5141.

Wessel, P., Luis, J.F., Uieda, L., Scharroo, R., Wobbe, F., Smith, W.H.F. & Tian, D., 2019. The Generic Mapping Tools version 6. *Geochem. Geophys. Geosyst.,* **20,** 5556–5564.

Yang, B.B., Gao, S.S., Liu, K.H., Elsheikh, A.A., Lemnifi, A.A., Refayee, H.A. & Yu, Y., 2014. Seismic anisotropy and mantle flow beneath the northern Great Plains of North America, *J. geophys. Res.,* **119**(3), 1971–1985.

Yang, B.B., Liu, Y., Dahm, H., Liu, K.H. & Gao, S.S., 2017. Seismic azimuthal anisotropy beneath the eastern United States and its geodynamic implications, *Geophys. Res. Lett.,* **44**(6), 2670–2678.

Yang, X., Li, H., Li, Y., Lü, Q., Zhang, G., Jiang, G. & Li, X., 2019. Seismic anisotropy beneath eastern China from shear wave splitting, *Geophys. J. Int.,* **218**(3), 1642–1651.

Zhang, S. & Karato, S.-I., 1995. Lattice preferred orientation of olivine aggregates deformed in simple shear, *Nature,* **375**(6534), 774–777.

Zhao, L., Zheng, T., Chen, L. & Tang, Q., 2007. Shear wave splitting in eastern and central China: implications for upper mantle deformation beneath continental margin, *Phys. Earth planet. Inter.,* **162**(1–2), 73–84.

Zhao, L., Zheng, T., Lu, G. & Ai, Y., 2011. No direct correlation of mantle flow beneath the North China Craton to the India–Eurasia collision: constraints from new SKS wave splitting measurements, *Geophys. J. Int.,* **187**(2), 1027–1037.

Zhao, L., Zheng, T. & Lu, G., 2013. Distinct upper mantle deformation of cratons in response to subduction: constraints from SKS wave splitting measurements in eastern China, *Gondwana Res.,* **23**(1), 39–53.

Zheng, X.F., Yao, Z.X., Liang, J.H. & Zheng, J., 2010. The role played and opportunities provided by IGP DMC of China National Seismic Network in Wenchuan earthquake disaster relief and researches, *Bull. seism. Soc. Am.,* **100**(5B), 2866–2872.

SUPPORTING INFORMATION

Supplementary data are available at *GJI* online.

Table S1. The resulting individual splitting measurements. This table lists all the individual splitting measurements shown in Figs 4–6 of the main text. The fields of the table include:

1) Number: Sequence number

2) Station: Station name

3) Phase: Seismic phase used for analysis (SKS, SKKS or PKS)

4) Event: Name of the seismic event (EQyydddhhmm, where yy is the year of the event, ddd is the day of year, hh and mm are the hour and minute)

5) St-lat.: Station latitude (deg.)

6) St-lon.: Station longitude (deg.)

7) ϕ: Fast orientation in degrees (clockwise from the North)

8) STD of ϕ: Standard Deviation (SD) of the fast orientation

9) δt: Splitting time in seconds
10) STD of δt: SD of the splitting time
11) BAZ: backazimuth of the event
12) BAZ90: Modulo-90° BAZ
13) BAZ180: Modulo-180° BAZ
14) Ev-Lat.: Event latitude (deg.)
15) Ev-Lon.: Event longitude (deg.)
16) Ev-Dep.: Focal depth in kilometres
17) Rank: Ranking for the measurement

Table S2. Real teleseismic and synthetic SWS measurements. This table lists all the individual splitting measurements shown in Fig. 9 of the main text. The fields of the table include:
1) Station: Station name
2) Event: Name of the seismic event (EQyydddhhmm, where yy is the year of the event, ddd is the day of year, hh and mm are the hour and minute)
3) Type: Type of the individual measurement (real teleseismic data or synthetic data)
4) Phase: Seismic phase used for analysis (SKS, SKKS, PKS or direct S)
5) ϕ (°): Fast orientation in degrees (clockwise from the North)
6) σ_{ϕ}(°): Standard Deviation (SD) of the fast orientation
7) δt (s): Splitting time in seconds
8) $\sigma_{\delta t}$(s): SD of the splitting time
9) BAZ: backazimuth of the event
10) p: Ray parameter in seconds/degree